Analysis of Counterparts of the Neutrino IceCube-200615A in the eFEDS Field of eROSITA

Lenz Oswald

2301672

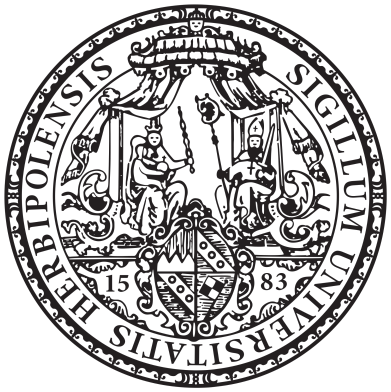

Bachelor Thesis

Institut für Theoretische Physik
und Astrophysik
Universität Würzburg

Supervisor: Prof. Dr. Sara Buson

Würzburg, 30.10.2021

Contents

Abstract

Active Galactic Nuclei (AGN) are very interesting sources in the extragalactic sky. They are the most luminous persistent objects. They are powered by a supermassive black hole (SMBH) in the center that is accreting the mass in its vicinity. This leads to the creation and emission of photons all across the electromagnetic spectrum through different processes. Thus, they are targets for a lot of different missions that collect data at all frequencies. An important distinction within different types of AGN is the presence of a relativistic jet that most likely origins near the black hole. It consists of highly relativistic particles like electrons and possibly protons. Multi-messenger astronomy is a branch in astronomy that deals with different ways to probe astrophysical objects in addition to photons. These include cosmic rays (charged particles that interact with the atmosphere and create air showers of secondary particles), gravitational waves and most importantly neutrinos. There are mechanisms in AGN that are promising to generate neutrinos like photomeson production in the jet.
This work focuses on a neutrino detected by the IceCube Observatory at the south pole (i.e. IceCube-200615A) that is within the eROSITA Final Equatorial Depth Survey (eFEDS). This region of the sky was chosen by the eROSITA mission as a test region before the start of their all-sky survey because of the good multi-wavelength coverage. The neutrino positional error region was searched for known radio-loud sources. This was done with the help of the catalogs WIBRaLS, KDBLLACS and 55BZCat. The source WISE J093141.09+023616.2 is listed by WIBRaLS as a flat-spectrum radio quasar (FSRQ) and this is the source, this work will focus on.
A spectral energy distribution (SED) across all frequencies was created with data from many different instruments in order to obtain more information about the object. Figure 11 shows the SED of the object and a steep rise in the radio band can be seen which indicates that a jet is present. Section 4.4 also deals with the origin of the emission at other frequencies like the optical and X-rays. To get a better look at the γ-ray regime, an analysis of the *Fermi*-LAT data was done to estimate the flux at these energies in section 4.3. Since no object was found in the latest *Fermi* catalog 4FGL-DR2 and no photon excess was measured, a flux upper limit was calculated to be $S_\gamma = 1.4 \times 10^{-12} \frac{\text{erg}}{\text{cm}^2\text{s}^1}$.
There are many additional aspects of the object that can be analyzed like the optical spectrum that is not available or estimating the luminosity of the object which provides information about the intrinsic properties of the central engine for example. Furthermore, there are a few more candidate radio-loud AGN that are slightly outside the positional error region of the neutrino and may be worth a further investigation as potential neutrino emitters. These methods are shown in section 5.

Zusammenfassung

Aktive Galaxiekerne (AGK) sind sehr interessante Quellen im extragalaktischen Himmel. Sie stellen die leuchtstärksten dauerhaft emittierenden Objekte im Universum dar. Angetrieben werden sie durch ein supermassives schwarzes Loch im Zentrum der Galaxie, das Masse in seiner Umgebung akkretiert. Dies führt zur Produktion und Ausstrahlung von Photonen in allen Bereichen des elektromagnetischen Spektrums. Daher sind sie auch Ziel von unterschiedlichsten Missionen in allen Frquenzbereichen. Eine wichtige Unterteilung der AGK ist die Präsenz eines relativistischen Jets der seinen Ursprung wahrscheinlich in der Nähe des schwarzen Loches hat. Er besteht aus hoch relativistischen Teilchen wie Elektronen und Protonen. Multi-Messenger Astronomie ist ein Teilbereich der Astronomie, der sich neben Photonen auch mit anderen Möglichkeiten beschäftigt astrophysikalische Objekte zu untersuchen. Dazu gehört kosmische Strahlung (geladene Teilchen die mit der Atmosphäre wechselwirken und Air-Showers aus Sekundärteilchen auslösen), Gravitationswellen und am allerwichtigsten für diese Arbeit: Neutrinos. Es gibt Prozesse in AGK die vielversprechend sind, wenn es um die Produktion von Neutrinos geht (Produktion von Photomesonen im Jet).
Diese Arbeit konzentriert sich auf die Neutrinodetektion IceCube-200615a, detektiert vom IceCube Neutrino Observatorium am Südpol. Diese Detektion befindet sich im Bereich der eROSITA Final Equatorial Depth Survey (eFEDS). Dieser Bereich am Himmel wurde von der eROSITA Mission als Testregion ausgewählt, da er eine sehr gute Abdeckung in vielen Wellenlängenbereichen durch andere Instrumente liefert. Der Positionsfehlerbereich der Neutriondetektion wurde nach bekannten radio-lauten Quellen abgesucht. Dazu wurden die Kataloge WIBRaLS, KDBLLACS und 5BZCat zu Hilfe genommen. Die Quelle WISE J093141.09+023616.2 ist in WIBRaLS als Flachspektrum Radio-Quasar aufgeführt und auf diese Quelle wird sich diese Arbeit fokussieren.
WIBRaLS ist jedoch stark durch Objekte wie radio-leise Objekte verunreinigt.
Eine Spektralenergieverteilung (SEV) mit Daten von verschiedensten Instrumenten in allen Frequenzbereichen wurde erstellt um mehr Informationen über die Quelle zu erhalten. Graphik 11 zeigt die SEV des Objekts und man kann einen steilen Anstieg im Radioband erkennen. Dies ist ein Zeichen dafür, dass es sich tatsächlich um einen radio-lauten AGK handelt. Kapitel 4.4 behandelt auch den Ursprung der Emission bei anderen Frequenzen wie im Optischen und Röntgenbereich. In Kapitel 4.3 wurde eine *Fermi*-Analyse durchgeführt um den Fluss bei diesen Energien abschätzen zu können. Da in dem neuesten *Fermi*-Katalog 4FGL-DR2 kein Objekt an dieser Stelle gelistet ist und kein Photonenüberschuss gemessen wurde, wurde ein Flussmaximum $S_\gamma = 1.4 \times 10^{-12} \frac{\text{erg}}{\text{cm}^2\text{s}^1}$ errechnet.
Es gibt noch viele andere Aspekte des Objekts, die analysiert werden können, wie zum Beispiel das optische Spektrum oder die bolometrische Leuchtkraft des Objekts, über die man Informationen über die Eigenschaften des schwarzen Loches bestimmen kann. Zusätzlich gibt es noch viele weitere AGK die sich im Positionsfehlerbereich des Neutrions befinden die potentielle Quellen darstellen.

1 Active Galactic Nuclei

1.1 Structure and Classification

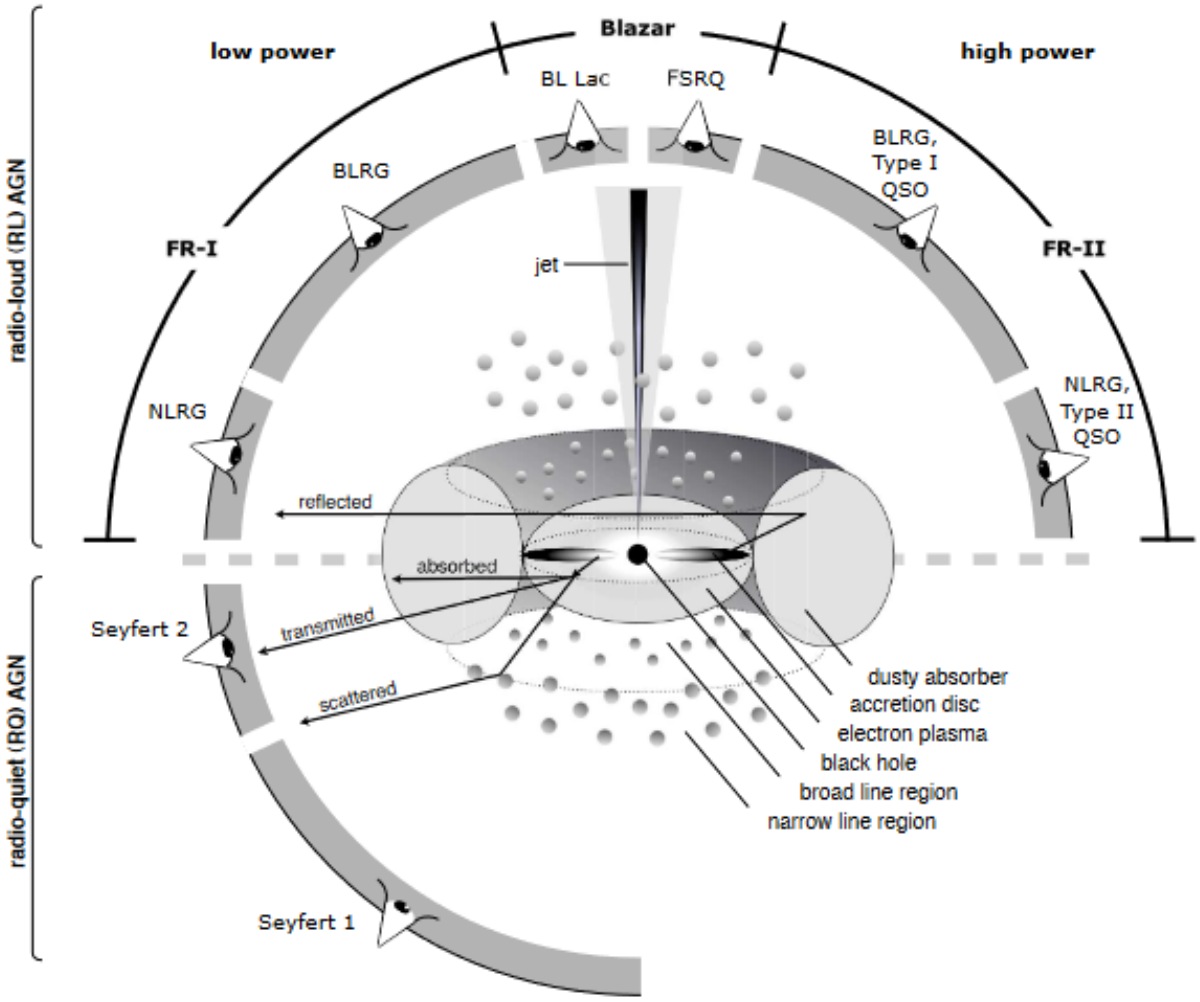

Figure 1: AGN unification model adopted from Beckmann and Shrader (2013). The center of the plot shows the structure of an AGN with the different regions that emit radiation. The lower half of the plot displays the radio-quiet AGN and the upper part shows the types of AGN that are defined as radio-loud. The angle under which the AGN is observed is shown by the eye indicator. This determines the type of AGN.

The most luminous persistent objects in the Universe are active galactic nuclei (AGN). AGN are powered by spinning supermassive black holes that are located in the center of galaxies and emit energy by accreting mass into the black hole. This radiation spans the whole electromagnetic spectrum. Figure 1 shows the unification model of AGN created by Beckmann and Shrader (2013). The center of the plot describes the structure of

the AGN with the black hole in its center. The gravitational potential energy of matter is converted into kinetic energy by it falling into the black hole. However, since the angular momentum has to be conserved, the matter starts rotating and a disk of accreting mass forms around the black hole. In the disk, the matter starts heating up through turbulent processes and emits thermal radiation. Further away from the black hole, there are clouds of dust, namely the broad- and narrow line region. They are responsible for emission lines in the optical spectrum. Surrounding the central black hole, a torus of gas and dust lies in the plane of the accretion disk. This torus absorbs a lot of radiation from the center and obscures the sight depending on the viewing angle.
AGN are mainly separated into radio-loud and radio-quiet AGN. The decisive quantity for this is the radio-loudness. It is defined as the ratio of the flux in the radio band ($\nu = 5\,\mathrm{GHz}$) to the flux in the optical B band at a wavelength of ~ 4400Å. (Urry and Paolo Padovani, 1995)

$$\frac{F_{5\,\mathrm{GHz}}}{F_B} \geq 10 \tag{1}$$

Radio-loud AGN typically have a jet of relativistic particles that dominates the emission. The jet originates from the black hole and points perpendicularly to the accretion disk in both directions. The collimated jet can reach a length of up to several $100\,\mathrm{kpc}$.

Plotting the flux density of an object as a function of the frequency of the radiation, the spectral energy distribution (SED) is obtained. Figure 2 shows the SED of different types of AGN. It also shows the origin of the emission in the different energy bands. The SED of non-jetted AGN consists of the emission of the different components like the accretion disk in the X-rays. The resulting SED of a non-jetted AGN is shown as a thick black line. Jetted AGN are dominated by the jet emission and the final SED shows almost no sign of the emission from other components which can be seen in figure 3. In the radio band, there is a distinct difference between jetted and non-jetted AGN. Jetted AGN show a very steep increase whereas non-jetted AGN show a very slow increase that steepens at higher frequencies.

1.2 Blazars

Figure 1 also shows how the classification of AGN is dependant on the angle under which it is observed. Most important for this work are blazars. Blazars are radio-loud AGN with a jet that is aligned with the line of sight of the observer. There are two types of blazars: Flat Spectrum Radio Quasars (FSRQ) that have broad emission lines in the optical spectrum and BL Lac objects that show a featureless spectrum in the optical and are typically fainter in the radio band than FSRQs.
Characteristic for both types of blazars is the double hump structure in their SED that can be seen in figure 3.

The first hump is caused by synchrotron emission from the charged particles in the relativistic jet. It is located at far UV frequencies up to the X-ray regime. Depending on

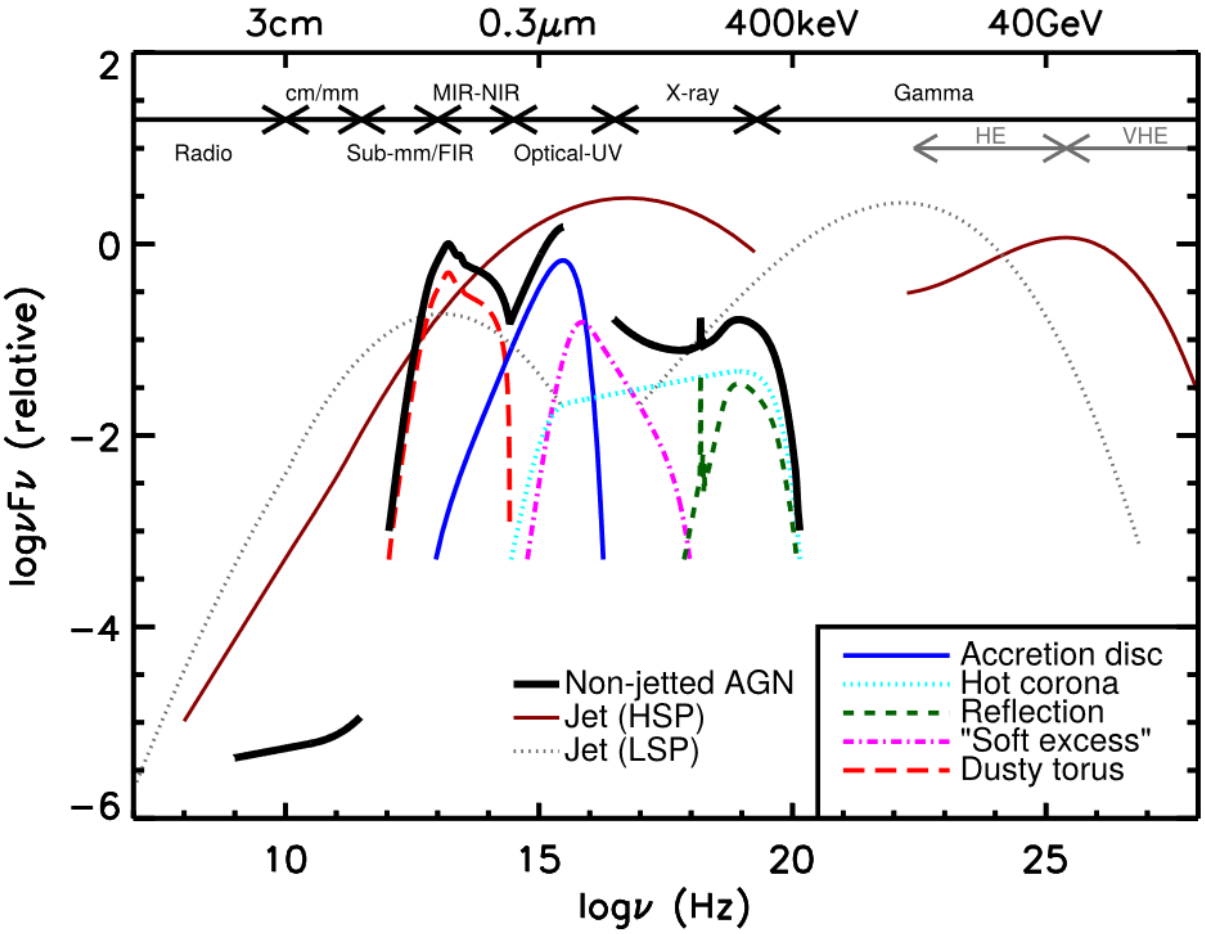

Figure 2: General spectral energy distribution of an AGN from P. Padovani et al. (2017). It shows the difference in the SEDs of the different types of AGN. For Example the thick red line and the dotted grey line show the emission of the jet of HSP and LSP blazars respectively. The SED of those objects is dominated by the jet emission. The colored lines show the emission that originates from the different parts of the AGN. In the case of a non-jetted AGN the resulting SED only consists of these parts. This results in a SED looking like the thick black line.

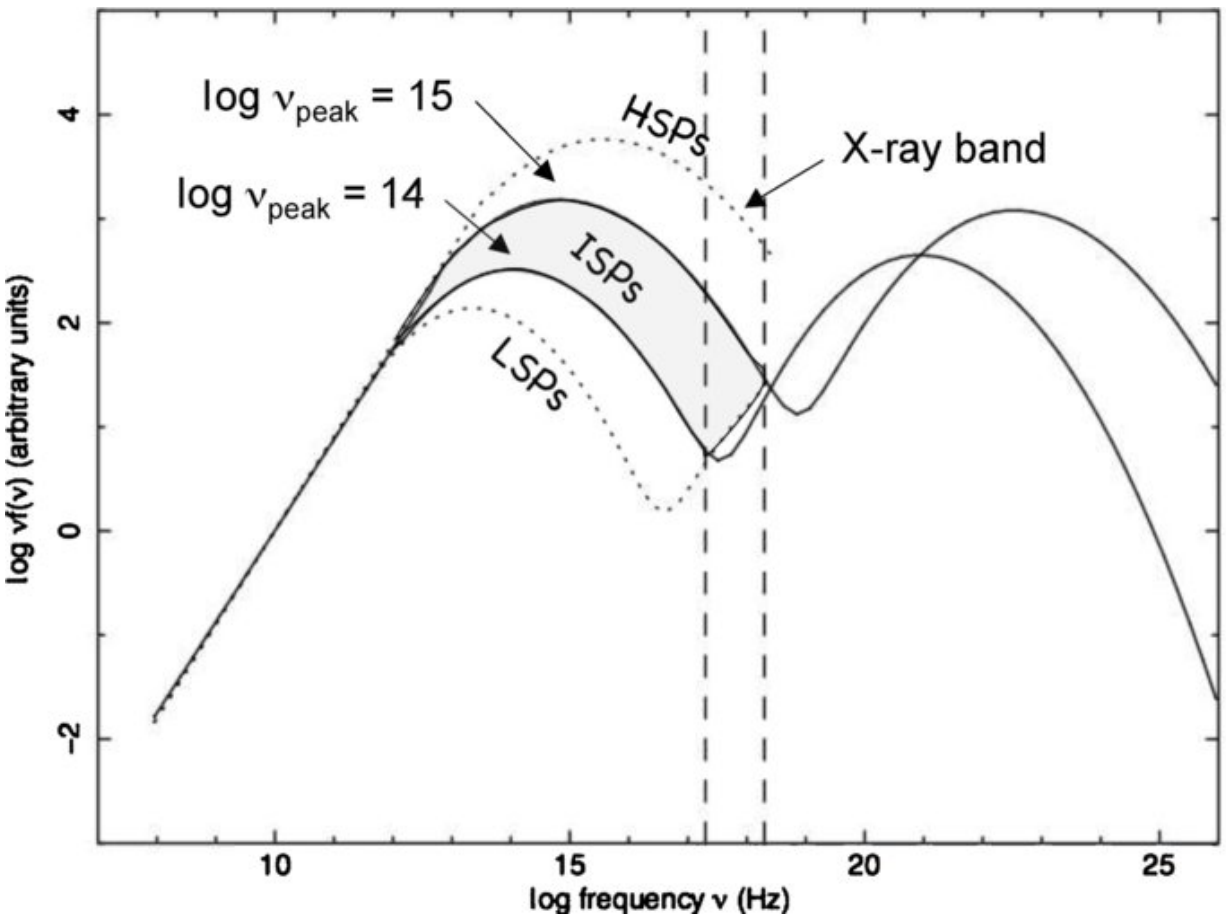

Figure 3: Spectral energy distribution of a typical blazar adapted from Abdo et al. (2010). The first hump is the synchrotron peak at far ultraviolet to X-ray frequencies. The origin of the second hump is not known. It lies at X-ray to the γ-ray frequencies. Jetted AGNs can be divided into three subclasses depending on the position of the synchrotron peak. Low synchroton peaked AGN (LSPs) for a peak frequency $\nu_{peak} < 10^{14}$ Hz, intermediate synchrotron peaked AGN (ISPs) for peak frecuencies 10^{14} Hz $< \nu_{peak} < 10^{15}$ Hz and high synchrotron peaked AGN (HSPs) for peak frequencies $\nu_{peak} > 10^{15}$ Hz

the frequency of the synchrotron peak, radio-loud AGN can be classified as low synchrotron peaked (LSPs) or high synchrotron peaked (HSPs). A LSP has its synchrotron peak at a peak frequency $\nu_{peak} < 10^{14}$ Hz, a HSP at $\nu_{peak} < 10^{15}$ Hz. AGNs with a peak frequency between these values are called intermediate synchrotron peaked (ISPs) as shown in Abdo et al. (2010). Typical SED shapes of the different types are shown in figure 3.
The origin of the second hump is still subject of research. There are leptonic models that describe the hump as the inverse Compton scattering of the synchrotron photons on the charged particles that created them. This is referred to as the synchrotron self Compton model (SSC). The other suggestions are hadronic models that discuss protons or heavier nuclei in the jet as the source for the radiation.
The Universe is constantly expanding, which means everything is getting farther away from each other. An exception from that are gravitationally or electromagnetically bound systems like galaxies or atoms. Photons on the other hand are affected by the expansion. This leads to a growing wavelength the longer the photons travels. The resulting redshift z is a measure of how far an object is away. It can be determined spectroscopicly if the optical spectrum has been measured. The emission lines of certain elements or molecules are always at the same rest frame wavelength. If the object originating this lines is located at a high redshift, the emission lines will be shifted to a higher wavelength due to the Doppler effect. This shift can be measured and used to calculate the distance to the object. If the optical spectrum of an object is not available, the redshift is estimated using photometric methods. This can be done for instance with a χ^2 test to compare the expected SED to the observed data.

1.3 *Fermi* Large Area Telescope

One telescope that observes blazars in the γ-ray band is the Large Area Telescope (LAT) on board of the *Fermi Gamma-ray Space Telescope*. The LAT went online on August 13 2008 and is since then scanning the sky in an all-sky survey. One survey takes the instrument ∼3 hours. It observes the sky at energies between 20 MeV and 300 GeV. At low energies up to 100 MeV however, the effective area is low. The LAT is an imaging, wide-field-of-view telescope that detects γ-rays through pair-production (Atwood et al., 2009). It consists of a 4 x 4 array of detectors that can be seen in figure 4. The $e^- - e^+$ production takes place in the converter-tracker module that consists of tungsten because the conversion probability is proportional to the atomic number $\propto Z^2$.

The analysis of *Fermi*-LAT data is done with the help of the python package Fermipy. It performs the data and model preparation with commands like 'gtmktime' and 'gtselect'. Furthermore it helps finding new source candidates in the region of interest or localize and fit the spatial extension of a source. For this work the version Fermipy 1.0.1 was used.

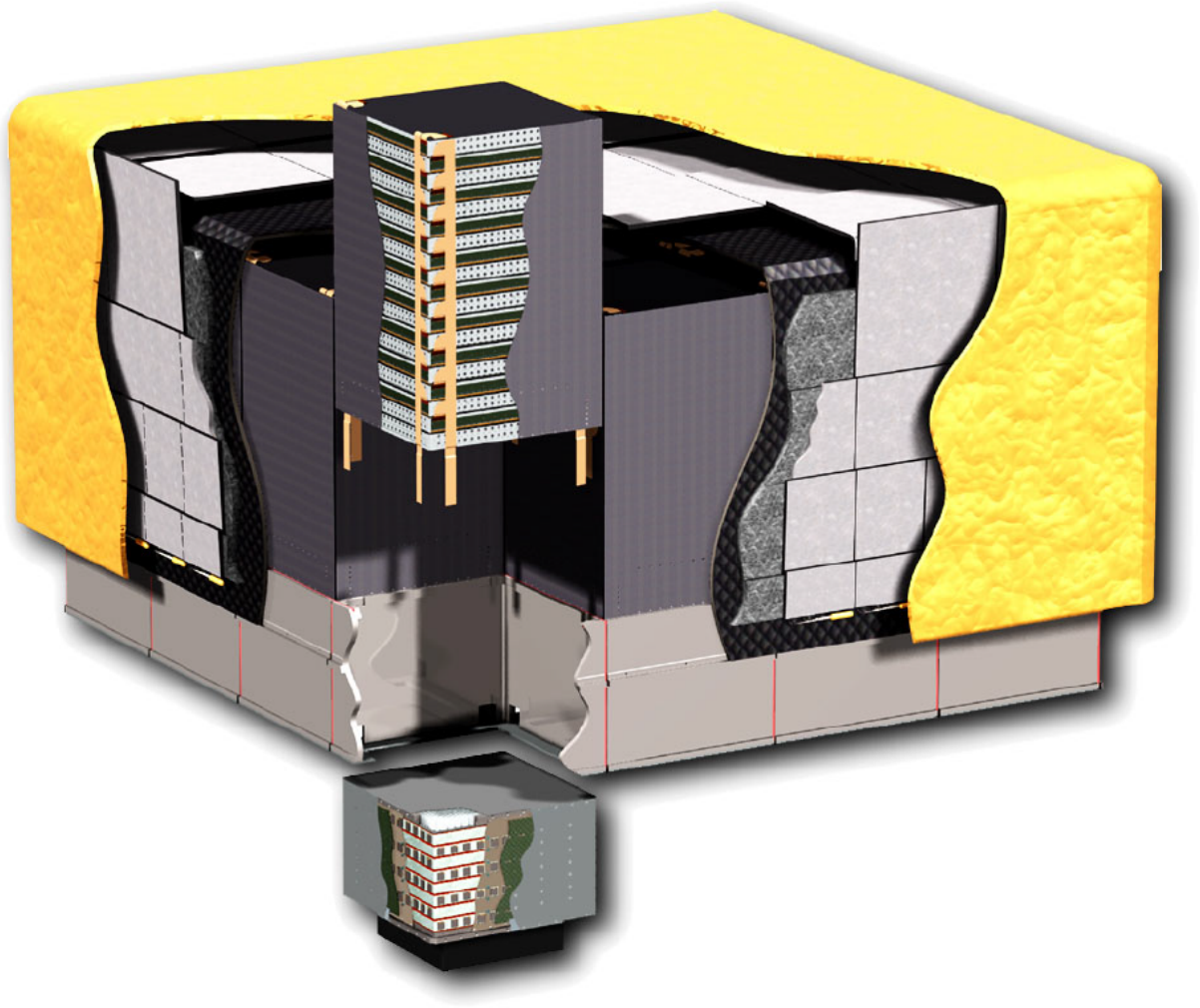

Figure 4: Tower array of the *Fermi*-LAT adapted from Atwood et al. (2009). The schematic shows one of the towers in detail. It consists of multiple layers of tungsten since heavy elements facilitate the production of electron-positron pairs.

2 Multi-messenger Astronomy

In multi-messenger astronomy, not only photons are observed as probes of astrophysical objects. Other ways to probe objects are cosmic rays, gravitational waves and neutrinos.
Cosmic rays are charged particles like protons and ions. Their origin is still being researched. They interact with atoms and molecules in the atmosphere and create air showers of secondary particles. Gravitational waves are ripples in the curvature of space-time that are created by cosmological events like the merging of black holes. They can be detected by interferometer experiments like the Laser Interferometer Gravitational-waves Observatory (LIGO) in Nort America and the Laser Interferometer Space Antenna (LISA) that is planned to launch in the early 2030s. Most important for this work are neutrinos. In 2017, a candidate-neutrino detection coincided with an active phase of the blazar TXS 0506+056. The subsequent multi-wavelength study lead to a significance of $3.5\,\sigma$ for the neutrino to come from the direction of TXS 0506+056 (IceCube Collaboration et al., 2018). This put forward blazars as a promising source class of extragalactic neutrino emitters.

2.1 Neutrinos

Neutrinos are elementary particles in the standard model of particle physics. They are chargeless leptons with a spin of $s_\nu = 1/2$, therefore they are fermions. There are three flavours of neutrinos corresponding to their lepton counterparts, the electron-neutrino, the muon-neutrino and the tauon-neutrino.
Since neutrinos do not have a charge, they do not interact with other particles through the electromagnetic force. They are also unaffected by the strong nuclear force and therefore only interact with other particles through the weak nuclear force. This leads to a mean free path λ for neutrinos depending on the neutrino energy that is much larger than the radius of the Earth. This makes the detection of neutrinos a difficult process.
On Earth, neutrinos are produced in nuclear reactors as a result of decaying atomic nuclei or in particle accelerators. Non human-made neutrinos are produced by the Sun or when cosmic rays interact with the atmosphere. More interesting for this work are extragalactic neutrinos with much higher energies (TeV-PeV). Their origin is still being researched and since the before mentioned TXS 0506+05 neutrino, blazars are promising sources of high-energy neutrinos. The production most likely happens in the jet of the AGN. There, hadronuclear (pp) and photohadronic ($p\gamma$) processes create π-mesons that in the end decay into neutrinos (Murase, Guetta, and Ahlers, 2016). Equations 2 and 3 describe the production of π-mesons and their decay into neutrinos.

$$p + \gamma \rightarrow \Delta^{\pm} \rightarrow \begin{cases} \pi^0 + p \\ \pi^{\pm} + n \end{cases} \tag{2}$$

$$\pi^{\pm} \rightarrow \mu^{\pm} + \nu_{\mu}(\bar{\nu_{\mu}}) \rightarrow e^{\pm} + \nu_{e}(\bar{\nu_{e}}) + \bar{\nu_{\mu}} + \nu_{\mu} \tag{3}$$

π^0-mesons decay into high-energy γ-rays that further tightens the connection to the TXS 0506+056 γ-ray blazar (Katz and Spiering, 2012).

2.2 IceCube Neutrino Observatory

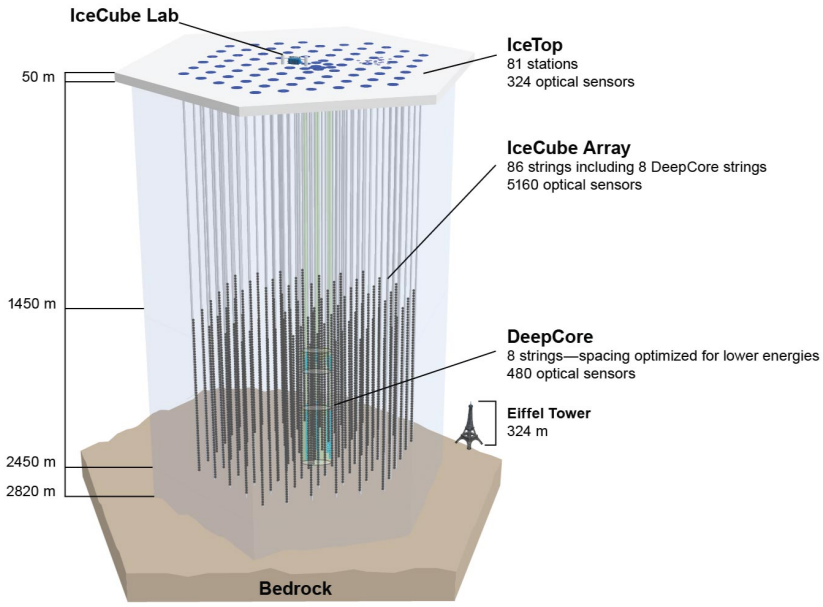

Figure 5: Structure of the IceCube Neutrino Observatory at the south pole, adopted from Aartsen et al. (2017). The observatory consists of 5160 Digital Optical Modules (DOMs) that are located between 1450 m and 2450 m. The DOMs detect the Cherenkov light emitted by a muon that is created when an incoming neutrino interacts with a nucleus in the ice.

In section 2.1 it was mentioned that neutrinos only interact with other particles through the weak nuclear force, which leads to very small cross-section. Therefore, the detection of neutrinos requires a instrument with a large volume. In 2011 the construction of the IceCube Neutrino Observatory at the South Pole was completed. Its purpose is to detect astrophysical neutrinos (TeV to PeV) of all flavors and determine their origin in the sky. To do so, it consists of 5160 Digital Optical Models (DOMs) that are embedded into the ice at a depth between 1450 m and 2450 m as shown in figure 5. Additionally, The DeepCore module consists of 480 special DOMs that are positioned in a way to optimally detect neutrinos at energies ranging from 10 GeV to 100 GeV. There are two fundamental detection methods that form the signatures of neutrinos in IceCube. First, track-like events: When an incoming neutrino interacts with a nucleus in the polar ice, a muon is produced that moves through the surrounding ice with a velocity greater than the speed of light in ice. This leads to a cone of Cherenkov radiation along the track of the

particle. The Cherenkov photons are then detected by the DOMs. The DOM consists of a sphere, that inhabits a downward facing photomultiplier tube (PMT). The detected photons are processed at the main board of the DOM and sent to the laboratory at the surface. Above a muon energy threshold of 1 TeV, it constantly loses energy trough radiation, that has a strong statistical variability. This leads to a large energy error for track-like neutrinos.
The other typical neutrino signature is the detection of electromagnetic and hadronic showers resulting from the interaction of all flavor neutrinos with nuclei. These kind of events lead to a more spherical light detection in the DOM. The detected light output of the shower is directly dependant on the energy of the shower particles. This leads to a more precise reconstruction of the neutrino energy as Aartsen et al. (2017) suggests.
IceCube has a real time alert system implemented, so follow-up observations of the neutrino regions can be done swiftly. There are two kinds of alerts that specify the probability of the neutrino to be astrophysical. Gold alerts are neutrino alerts that have a probability of 50% or higher to be of astrophysical origin. There are ∼10 Gold alerts per year. Neutrinos that have a probability between 30 to 50% to be astrophysical are called Bronze alerts of which there are ∼30 per year.
After such an alert, there are several ground and space based instruments that follow-up the event. They are looking for sources that are within the neutrino positional error that could potentially be the source of the particle. It may be also interesting if the source has an unusual high flux in a specific energy band. Such flaring states are very interesting as potential neutrino sources since the exact mechanisms of how neutrinos are produced in astrophysical objects are still being researched.

2.3 Status of Art

As aforementioned, the blazar TXS 0506+056 was the first correlation of a detected neutrino and a blazar with a significance of $3.5\,\sigma$. The blazar was in a flaring state in the γ-ray regime and the production processes hint towards a correlation between the production of γ-rays and high-energy extragalactic neutrinos (IceCube Collaboration et al., 2018).
However, Yuan, Murase, and Mészáros (2020) suggests that neutrinos produced by γ-ray blazars are not the dominant fraction of the isotropic neutrino flux. There are several works that support the claim that blazars do not have to be active in the γ-ray band to be high-energy neutrino sources.

Plavin et al. (2021) suggests that high-energy neutrinos are produced within the central regions of radio-loud blazars. Figure 6 shows the production process of neutrinos in radio-loud blazars as described in Plavin et al. (2021). The relativistic electrons in the jet emit synchrotron radiation at radio energies. These photons undergo SSC scattering and their energy is increased to hard X-rays (keV-MeV). Relativistic protons can interact with the photons in the X-ray band and produce π-mesons via photohadronic processes.

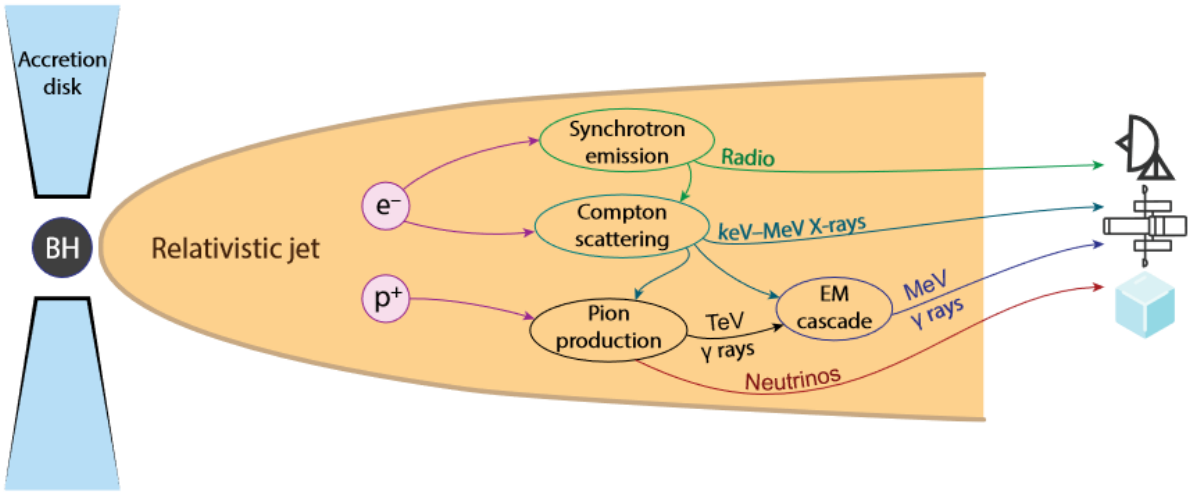

Figure 6: Relativistic electrons produce synchrotron emission in the radio band that is scattered to X-rays by synchrotron self Compton scattering. The higher energy photons can interact with relativistic protons in the jet to produce π-mesons that decay into neutrinos. Adapted from Plavin et al. (2021).

The decay of the π-mesons produce neutrinos that can be detected by IceCube and high-energy γ-rays in the TeV band.
Murase, Guetta, and Ahlers (2016) gives an explanation why these high-energy photons are not detected. The γ-rays interact with target photons in the object itself, undergo $e^- - e^+$ pair-production and can not escape the source. The high-energy photons that do escape the object, interact with photons on their way and create cascades that lead to photons that appear in the high keV to MeV band.
Mastichiadis and Petropoulou (2021) deals with the production of neutrinos in blazars in correlation with hadronic X-ray flares, which means blazars with a jet that contains relativistic protons. The synchrotron radiation emitted by these protons powers the X-ray flares. If the photons have a sufficient energy, they can interact with the protons and create π-mesons that decay into high-energy neutrinos. This process is also accompanied by MeV γ-rays and not detectable at higher energies.
These are just examples that encourage the search for neutrino counterpart blazars in the MeV and X-ray band. However, there are no missions that provide information at MeV energies. Therefore, it is helpful to look at the X-ray band to determine whether a blazar is a potential neutrino-rich source or not. This raises the need for good instruments and surveys that deliver data in these bands.

3 eROSITA and eFEDs

3.1 eROSITA

In 2019, the Spectrum-Roentgen-Gamma mission was launched and aboard is the Roentgen telescope extended ROentgen Survey with an Imaging Telescope Array (eROSITA). It is the successor telescope of the ROSAT mission which observed the sky in the 0.5 to

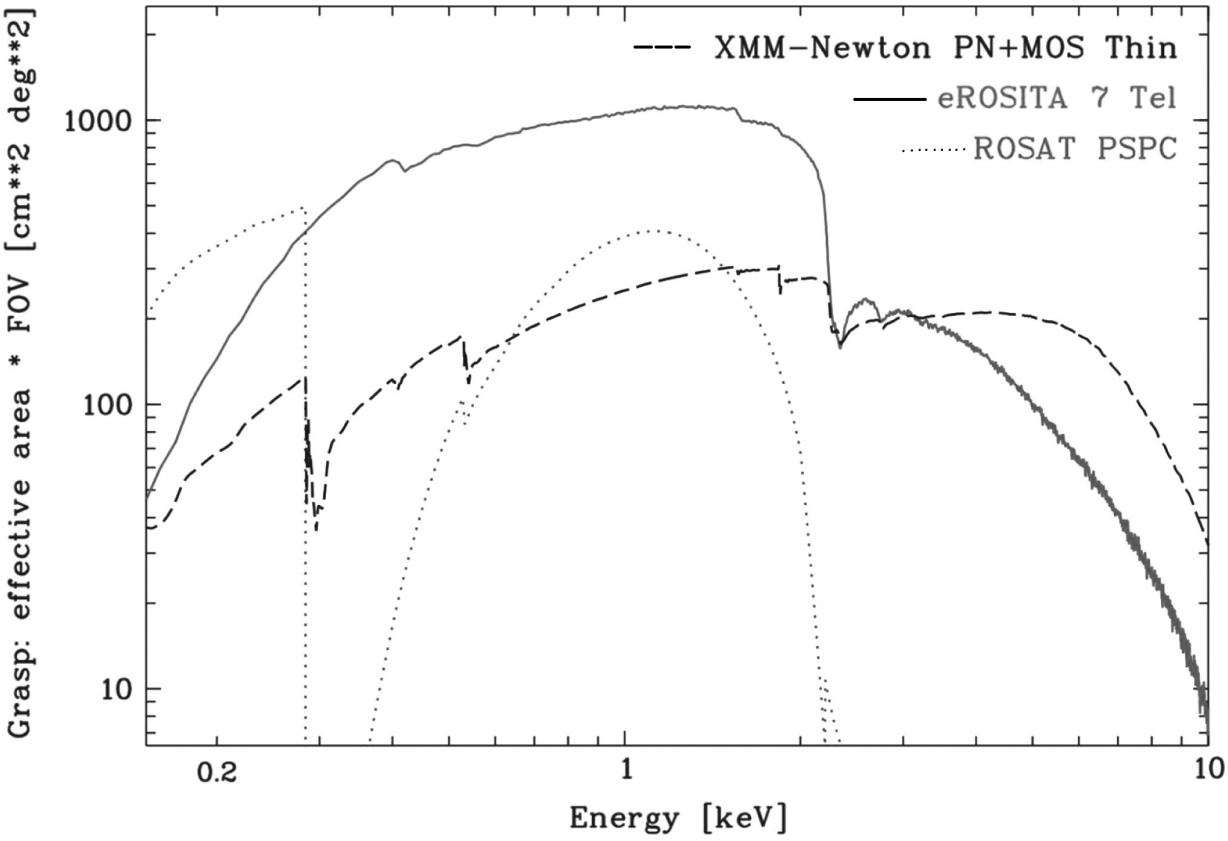

Figure 7: Effective are times the field of view plotted against the energy of the incoming photons. eROSITA (full line) compared to its predecessor ROSAT (dotted line) and another x-ray instrument XMM-Newton (dashed line). eROSITA performs better than the other two instruments in the energy band around 1 keV. ROSITA performs a little bit better at very soft x-rays but it has a gap at ≈ 0.3 keV and stops at ≈ 1.1 keV. XMM-Newton performs worse than eROSITA at all energies besides at hard X-rays. (Predehl, 2014)

2 keV band. eROSITA is about 30 times more sensitive at these energies and is able to additionally observe the X-ray regime up to 8 keV. For the first four years of its mission, eROSITA will do an all-sky survey, scanning the sky a total of eight times. After the all-sky survey, eROSITA will do three years of pointed observation. The main goal of the mission is to look for galaxy clusters and therefore study the large scale structures

of our Universe. Besides this, eROSITA will detect a large number of AGN (Predehl (2014) approximates about 3 Million AGN) that are especially interesting when looking for astrophysical neutrinos.
Figure 7 compares the grasp of eROSITA, which is the effective area times the field of view with two other missions: the predecessor instrument ROSAT and another X-ray instrument XMM-Newton. The Graph shows that eROSITA performs better than XMM-Newton in all energy bands except of the hard X-rays above 3 keV. ROSAT on the other hand does not even span the whole energy range and only performs at energies up to ≈ 0.3 keV and between ≈ 0.4 and ≈ 1.1 keV. This makes eROSITA the best operational mission to do an all-sky survey in the whole X-ray regime.
The instrument consists of seven identical X-ray telescopes that are positioned in a hexagonal shape. Each telescope is made of 54 mirror-shells that have a diameter of 360 mm and a common focal length of 1600 mm. Behind the mirrors, each telescope has a CCD-camera that has a field of view of $1^\circ.03$ (Predehl, 2014).

3.2 eFEDs

Before its planned all-sky survey, eROSITA observed a region of the sky for four days to test whether the instrument is working as planned. This region is called the eROSITA Final Equatorial Depth Survey (eFEDS). eFEDS can be seen in figure 8 with its area of 142 deg^2 and is centered at a right ascension RA $= 136^\circ$ and a declination Dec $= 1.5^\circ$. The reason this region of the sky was chosen as testing ground is that it provides one of the best multi-wavelength coverages for an extragalactic field of this size as Brunner et al. (2021) suggests. For example, it lies within an area that has very deep near infrared and optical imaging done by the KIDS-VIKING and DESI Legacy Imaging survey among others. Additionally, it was near the initial position of eROSITA so it was observable in the short time before the all-sky survey.
Brunner et al. (2021) reports a total count of 27910 X-ray sources in eFEDS. Among those, there are 21952 candidate AGN (T. Liu et al., 2021) which makes up 70% of the population. They are dominated by X-ray unobscured ($N_H < 21.5$) sources with a mean power-law slope of 1.94 ± 0.22. About 3% of the eFEDS sources are located at the edge of the field. These sources should be avoided for further analysis because they suffer from shorter exposure, higher vignetting and a higher background. The DESI Legacy Imaging Survey DR8 (Dey et al., 2019, LS8) was used to look for counterparts of the eFEDS sources in the optical. Two independent methods were used to analyse whether a source from LS8 is a counterpart or not (a Bayesian method and a maximum-likelihood analysis). If both methods agree on the same counterpart, the **CTP_quality** is greater or equal than three. These counterparts are safe for further analysis. If the methods find different counterparts, the counterpart is still reliable but there is a secondary counterpart candidate. These sources have a **CTP_quality**=2. Sources with a **CTP_quality** lower than 2 have no secure counterpart in the LS8 and are not taken into consideration for further analysis.
Another important difference between sources is whether they are positioned in our

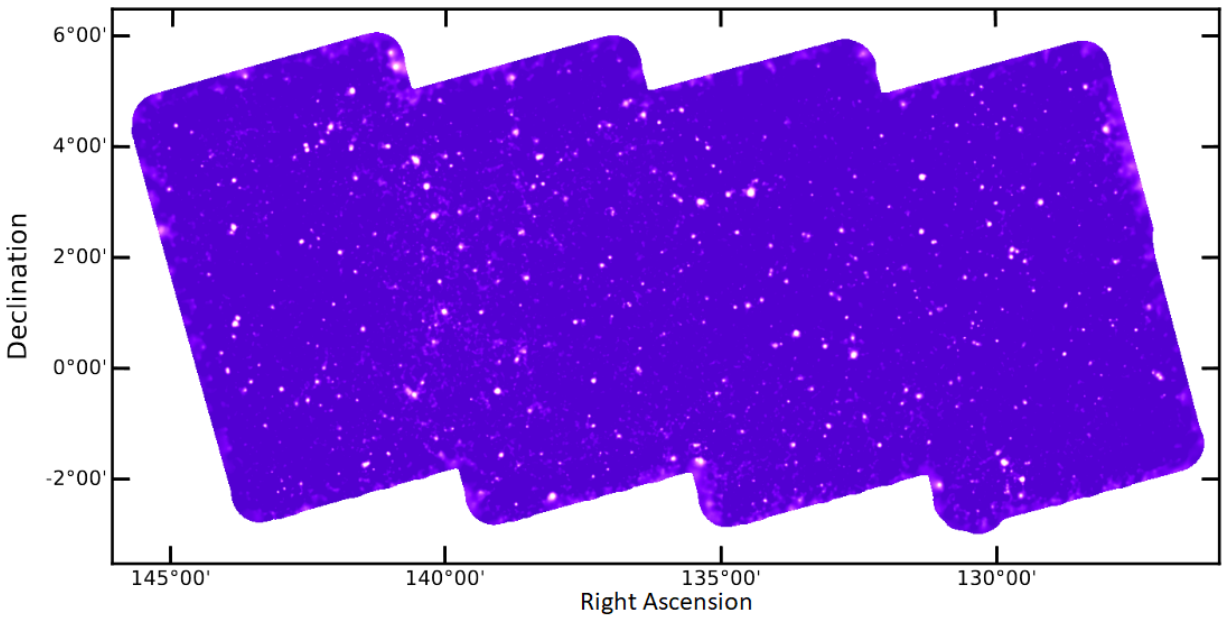

Figure 8: Picture of the eROSITA Final Equatorial Depth Survey (eFEDS). The region is centered at RA $= 136°$ deg and Dec $= 1.5°$ deg which results in an area of 142 deg^2. (Adapted from A. Liu et al. (2021))

local galaxy or are extragalactic. There are 2822 sources that are classified as either "Likely" or "Secure" galactic which are treated as stars. There is still a chance that there are extragalactic compact objects in this class mentions T. Liu et al. (2021). The redshift of the eFEDS objects was measured using the optical spectrum if available. These sources with spectroscopic redshift have a redshift grade $zG = 5$ (spec-z). In Salvato et al. (2021) the photometric redshift for the objects without optical spectrum are calculated. This is done using two different methods, a SED fitting method and a machine learning method. If both methods agree, $zG = 4$ for these kinds of sources which corresponds to a reliable redshift. Objects marked as galactic have $zG = 4$ by definition because both methods set their redshift to zero. If the methods disagree on a redshift, $zG < 4$ and not reliable. It has to be mentioned that photometric redshifts in general are not nearly as reliable as spectroscopic redshifts, especially for AGNs. When trying to find the redshift through SED fitting, each data point is redshift dependant because it consists of a flux of photons that experienced the redshift. Additionally, there are effects like dust extinction and variability which is a typical characteristic for AGN. This especially results in a problem when the data points are taken at different times since the flux is changing over time.

4 The Neutrino IceCube-200615A

4.1 Position in the eFEDS Field

On June 15 2020, the IceCube Observatory detected a neutrino at 14:49:17 Greenwich Mean Time. The position of the neutrino is RA $= (142.95\ ^{+1.18}_{-1.45})$ deg and Dec $= (3.66\ ^{+1.19}_{-1.06})$ deg. The error is the statistical error of the neutrino detection. Hovatta, T. et al. (2021) suggests that in addition to the statistical error Δ_{stat} of the neutrino, the systematic error $\Delta\psi$ of the observatory has to be taken into account. The resulting uncertainty is given by $\sqrt{\Delta^2_{\text{stat}} + \Delta\psi^2}$. The red ellipse in figure 9 shows neutrino positional error region with a systematic error of $\Delta\psi = 1$ deg. It is a Gold alert and therefore the energy of the neutrino is above 100 TeV. Interestingly, the neutrino lies within the eFEDS field which provides a good coverage in the X-ray regime. Furthermore, since

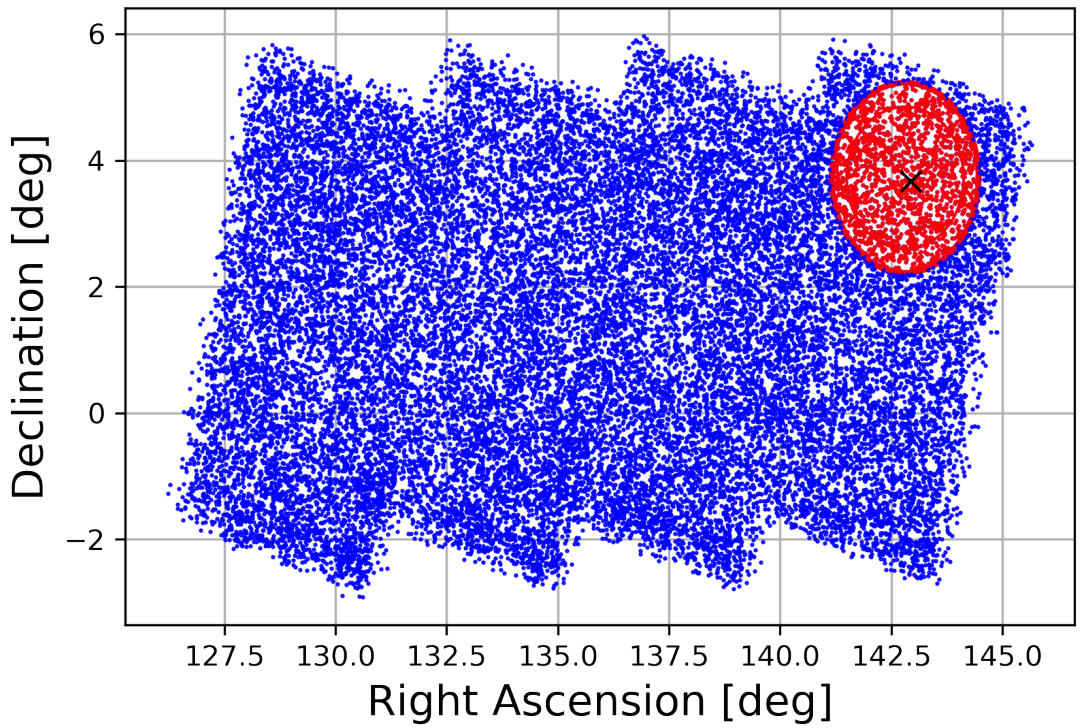

Figure 9: Plot of all eROSITA X-ray AGN in the eFEDS region (Blue squares). There are in total 21952 candidate AGN. The black cross in the upper right marks the position of the neutrino IceCube-200615A. The red ellipse around the neutrino detection is the positional error region of the neutrino with all eROSITA AGN marked with red squares.

the eFEDS field was specifically chosen because of its good multi-wavelength coverage, there are plenty of other instruments that provide information about objects within the field. Figure 9 shows the position of the neutrino IceCube-200615A in the eFEDS region which is the black cross in the upper right of the field. The blue squares indicate AGN that lie within the eFEDS field but not directly at the edge. The red squares mark eFEDS AGN that are within the neutrino positional error and are therefore potential counterparts for the neutrino detection.

4.2 Potential Counterparts

Name	RA [deg]	Dec [deg]	Sep. [deg]	Suggested Type
WISE J093141.09+023616.2	142.92121	+2.6045	1.06	FSRQ
WISE J092706.83+042722.1	141.77848	+4.4562	1.42	BL Lac
CRATES J092810+024118	142.04621	+2.6891	1.33	FSRQ
5BZQ J0924+0309	141.06125	+3.1502	1.96	FSRQ

Table 1: Candidate radio-loud objects near the neutrino detection IceCube-200615A. The separation is the distance from the object to the best position of the neutrino detection. This work focuses on the object WISE J093141.09+023616.2 because it is located closest to the neutrino. Column 1 shows the name of the object. Columns 2 and 3 show the coordinates. Column 4 shows the distance of the object to the neutrino detection IceCube-200615A and column 5 shows the type of AGN that is suggested by the corresponding catalog.

Out of all AGN in the error region, this work focuses only on the radio-loud (i.e. the jetted) objects. To check if an AGN is radio-loud or radio-quiet, the flux and therefore counterparts in the optical and in the radio band are needed (e.g. section 1). eROSITA and eFEDS in particular is a very deep survey compared to other missions and detects objects with a very faint flux. This results in many objects that are detected by eROSITA that do not have many counterparts in other bands. This makes the classification of the radio-loudness a hard task to accomplish. Fortunately, there are catalogs that focus on including radio-loud AGN like 5BZCat (Massaro et al., 2008) or WIBRaLS, KDEBLLACS (D'Abrusco et al., 2019) and CRATES (Healey et al., 2007).

In these catalogs, there are three objects that are within the neutrino positional error that are listed in table 1. Figure 10 shows the position of these objects. Although the 5BZCat source 5BZQ J0924+0309 is outside of the positional error region, it is still included in the table as an interesting source for further analysis because 5BZCat is a very pure catalog and the source is almost within the error. It is marked as a magenta cross in figure 10. The green cross marks the FSRQ CRATES J0982810+024118. The yellow cross indicates the position of the KDBLLACS BL Lac WISE J092706.83+042722.1. WISE

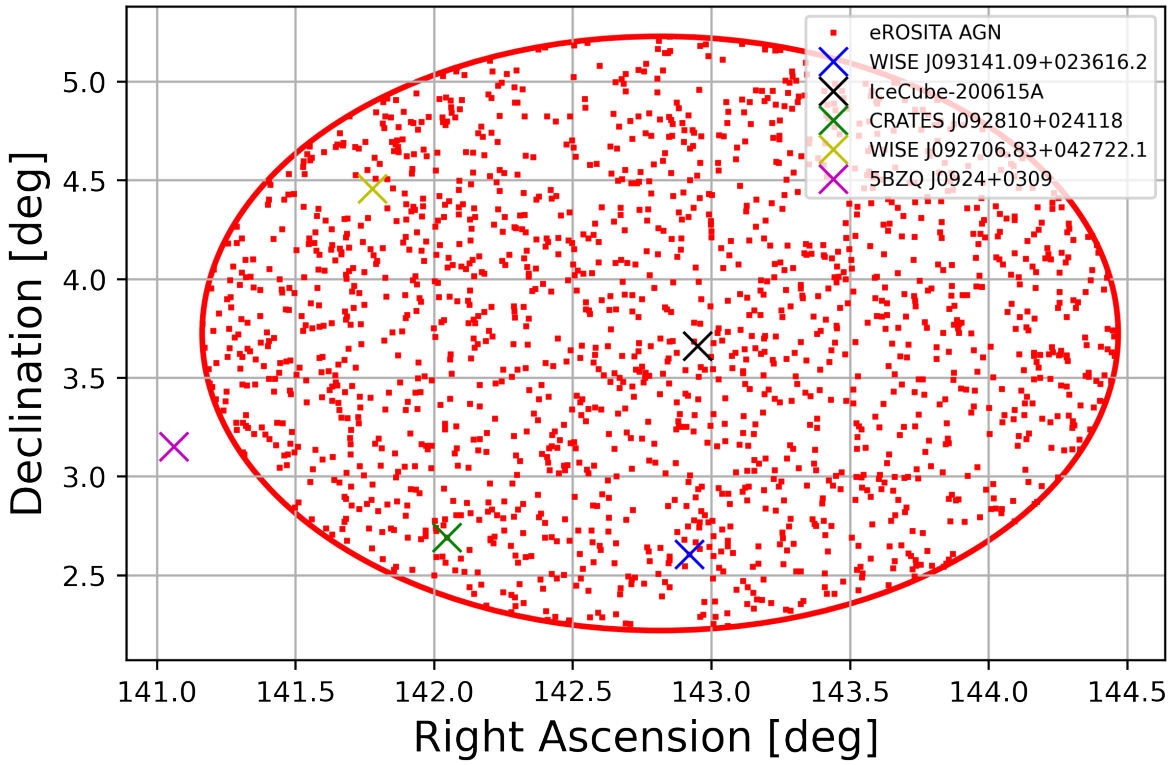

Figure 10: 90% neutrino positional error region. The black cross marks the best position of the neutrino IceCube-200615A. The red squares in the ellipse indicate AGN in the eFEDS region observed by eROSITA. The blue cross at the bottom edge of the error region marks the WISE source WISE J093141.09+023616.2. It is the closest object to the neutrino in this region and was chosen as primary subject for further analysis in this work. The other crosses mark candidate radio-loud sources from the catalogs 55BZCat, KDBLLACS, WIBRaLS and CRATES that are interesting for future analysis.

J0931341.09+023616.2 is marked as a blue cross at the bottom of the region. It is located at RA $= 142.9212$ deg and Dec $= 2.6045$ deg and is chosen as the primary subject of this work because it is closest to the neutrino detection. The red ellipse marks the edge of the 90% neutrino positional error region, i.e. the probability of the neutrino origin to be in this region is 90%. The black cross in the center indicates the best position of the neutrino IceCube-200615A. The red squares within the ellipse are AGN that are observed by eROSITA.
WISE J093141.09+023616.2 is listed in WIBRaLS as a possible blazar, more specifically a FSRQ. WIBRaLS is only a catalog of blazar candidates. However, Menezes et al. (2019) did an optical characterization of the objects in WIBRaLS and KDEBLLACS and came to the conclusion that 30% of the objects in WIBRaLS are secure blazars. There is a contamination of ∼60% by quasi-stellar objects (QSO). A significant amount of these QSOs may have a flat spectrum and therefore be FSRQs. This increases the amount of possible blazars to up to ∼80%. A way to make sure what kind of object is observed is to look at the SED since blazars show the typical double hump structure (e.g. in chapter 1). Figure 11 shows the SED of the object WISE J093141.09+023616. The data from the different instruments were taken from the corresponding catalogs and converted into the flux density unit erg cm^{-2} s^{-1}. Looking for counterparts of the WISE source in the eFEDS AGN catalog, results in one source. They are 1.75 arcsec apart which makes it very likely that the two sources are the same object. The object has a **CTP_quality** of 4 which provides a reliable counterpart in the optical LS8 catalog. Unfortunately, LS8 does not provide a spectrum for the source, neither does SDSS (Sloan Digital Sky Survey)(Blanton et al., 2017) nor LAMOST (Large Sky Area Multi-Object Fibre Spectroscopic Telescope)(Zhao et al., 2012). Thus, it is not possible to obtain a spectroscopic redshift value for the object and the unreliable photometric redshift $z = 1.914$ has to be used. eFEDS provides a value of the flux between 0.5 and 2 keV and between 2.3 and 5 keV that can be seen in figure 11. At the position of the source no object is listed in the latest catalog of the *Fermi*-LAT 4FGL-DR2. Therefore, a Fermipy analysis was done to check whether there is a faint signal or only an upper limit can be estimated.

4.3 *Fermi* Analysis

First, the data were collected from the *Fermi*-LAT in the region around the object. The region of interest is a square with a sidelength of 10 deg centered around the position of the WISE source. Only photons in the energy range from 0.1 to 300 GeV are used for the analysis. The data was further filtered by only taking into account events with an 'evclass = 128' and an 'evtype = 3'. This makes sure that the event is a photon that is detected either as a front or back event. The gtmaketime function of the *Fermi* Science Tools makes sure that the data are scientifically valid, i.e. that the data is taken only during good time intervals. Bad time intervals are for example when the instrument is above the South Atlantic Anomaly, where a great amount of charged particles results in very high fluxes that would saturate the detectors of the instrument and shorten the lifetime of the LAT. Reason for the anomaly is the geometry of the earth and its mag-

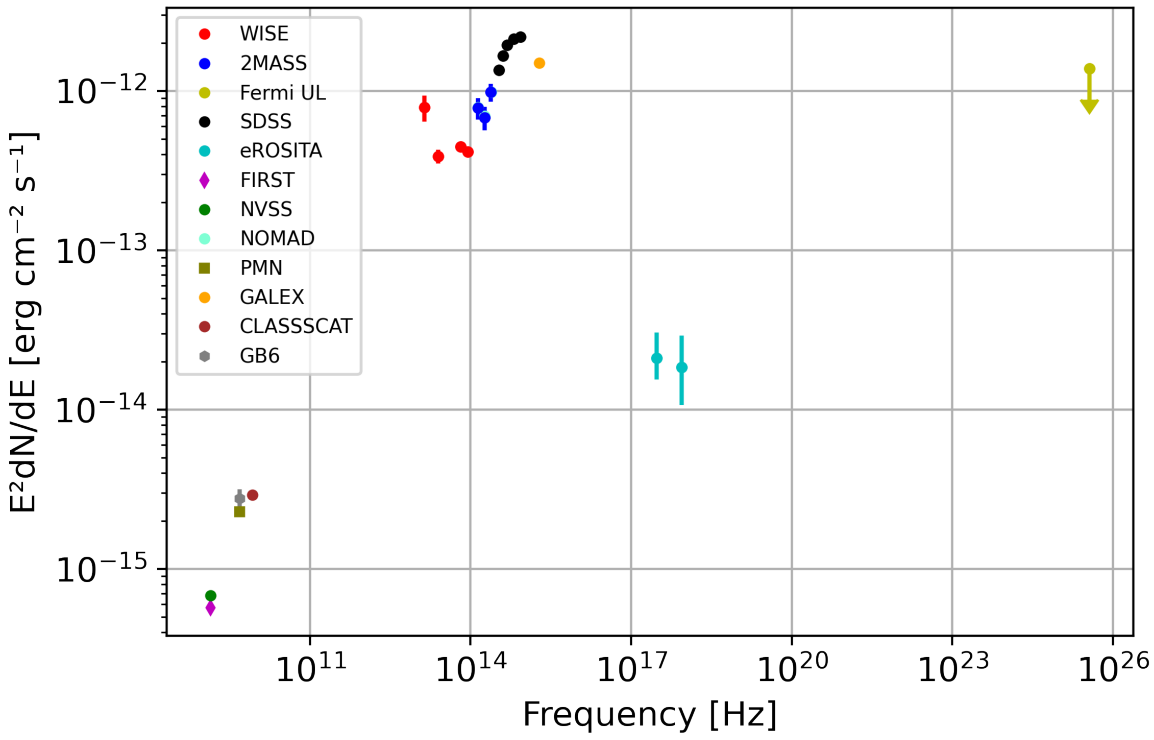

Figure 11: Spectral energy distribution of the object WISE J093141.09+023616.2. The data was taken from the corresponding catalogs. At this location, there are no *Fermi*-LAT sources in the 4FGL-DR2 catalog. Therefore a *Fermi* analysis was done at this location which yields an upper limit for the flux.

netic field.
In order to get only the good time intervals, the events with a 'DATA_QUAL > 0' and 'LAT_CONFIG = 1' are taken into account. Data at a zenith angle larger than 90 deg is also discarded. At high zenith angles, the data is contaminated with atmospheric γ-rays that are produced when cosmic rays interact with particles in the atmosphere. The next step in the *Fermi* analysis is to create a model that includes all the point sources in the region of interest. This is done by the Fermipy software that helps with the analysis of *Fermi* data. It creates a XML file that includes all the point sources within the region of interest from the *Fermi* catalog 4FGL (Abdollahi et al., 2020). It also includes the position, spectral type, and the values of the corresponding fit parameters. The model also contains information about the diffuse emission. There is the diffuse galactic emission that has its origin in cosmic rays that interact with interstellar light matter and low-energy photon fields in our galaxy. The extragalactic part is called diffuse isotropic emission. It is composed of unresolved astrophysical components (e.g. star formation galaxies and unresolved blazars), instrument residuals and possibly radiation from new physics (i.e. physical phenomena like dark matter).
Now, a maximum likelihood analysis can be done. Each pixel in the region of interest has an expcected number of counts from the model. The Poisson likelihood (Compare Eq. 4) to measure the observed number of counts in each pixel is computed.

$$f(n, \lambda) = \frac{\lambda^n}{n!} \mathrm{e}^{-\lambda} \tag{4}$$

$f(n, \lambda)$ is the probability that n counts are observed in a pixel in which the model predicts λ counts. The product of the probability of each pixel gives the likelihood that exactly as many counts are observed given a specific model. The likelihood is still dependent on a finite amount of free parameters that can be varied to get the maximum likelihood which is the best fit model.
There still are deviations of the observed data from the model. These deviations are shown in the residual map (Fig. 12a). It shows the difference of predicted counts to the observed counts in significances, i.e. how likely it is that such a deviation occurs. There are regions of low significance residuals which are scattered around the region of interest. They come from deviations in the diffuse emission and can be neglected as long as they are not clumped or significant. There are no spots in the region of interest with a significance higher than $\sim$3. This indicates that the model of the region of interest fits the data adequately.

Figure 12b shows the test statistic (TS) map of the region of interest with the object WISE J093141.09+023616.2 excluded from the model. The TS is a measure of how likely it is that a truly astrophysical signal is at a certain position.

$$\mathrm{TS} = -2 \log(\frac{L_{max,0}}{L_{max,1}}) \tag{5}$$

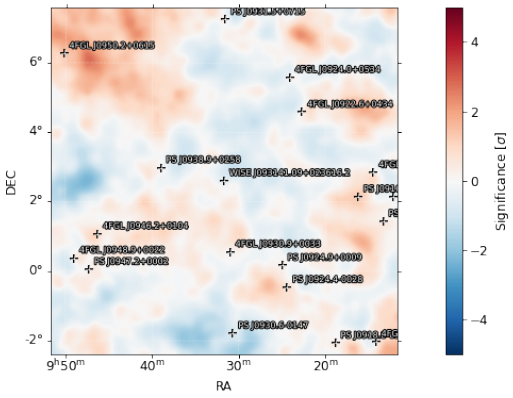

(a) Residual map of the region of interest. It shows the difference of counts in each pixel to the predicted counts of the model. The low significance spots of residuals are due to small variations of the diffuse emission. They can be neglected as long as they are not too big

(b) TS map of the region of interest. The test statistic (TS) is a measure how probable it is that an object is truly at a specific position. It compares the likelihood of a model where the object is excluded to the likelihood of a model with the object included.

Figure 12: Residual map and TS map of the region of interest around the WISE object J093141.09+023616.2 at RA $= 142.9212$ and Dec $= 2.6045$. The region of interest has a sidelength of 10 deg.

$L_{max,0}$ is the maximum likelihood value for the model without the object of interest. $L_{max,1}$ on the other hand is the maximum likelihood value with the object included in the model. Thus TS is a monotonically increasing quantity with growing $L_{max,1}$. A high value of TS means a high probability that a source is at that location. The TS at the center of figure 12b is close to zero. Therefore, it is very unlikely that there is an object that emits γ-radiation. An upper limit of the γ-ray photon flux was estimated to be

$$\mathrm{F}_\gamma = 1.1 \times 10^{-9} \, \frac{\text{photons}}{\text{cm}^2\text{s}}$$

The upper limit marks the flux density threshold the object has to emit to be detected by the *Fermi*-LAT. It depends on the position of the sky and the energy of the incoming photons because both affect the effectiveness of the instrument. This is determined by the Instrument Response Functions (IRFs).
This value can be used to calculate the γ-ray energy flux S_γ with the formula from G. Ghisellini, Maraschi, and Tavecchio (2009).

$$\mathrm{S}_\gamma = \mathrm{h}\nu_1 \mathrm{F}_\gamma \ln(\frac{\nu_2}{\nu_1}) \tag{6}$$

ν_1 and ν_2 are the frequencies between those the flux is determined and F_γ is the *Fermi* photon flux. The resulting energy flux for WISE J093141.09+023616.2 is calculated to be

$$S_\gamma = 1.4 \times 10^{-12} \frac{\text{erg}}{\text{cm}^2\text{s}}$$

which is shown in figure 11. The *Fermi*-LAT 4FGL-DR2 catalog includes all the data from 10 years of survey. There are several earlier catalogs with less data that have to be checked whether there is a source at this position. If the object is fainter today than it was up to the point 2FGL (2 years of data collection) was released, the overall flux density in the newest catalog will be lower than in 2FGL. Therefore, the catalogs 1FGL (1 year of data collection), 2FGL, 3FGL (4 years of data collection) and 4FGL (8 years of data collection) were checked whether a source is located in correlation with WISE J093141.09+023616.2. No catalog included a source within the 95% confidence region of *Fermi*.
Additionally, the Energetic Gamma Ray Experiment Telescope (EGRET) catalog was checked. It also did not yield an object. This further consolidates that the upper limit determined by this work is the highest flux density the object can have over the last 13 years of time integration. Otherwise, it would have been detected by one of the missions and included in one of the checked catalogs.

4.4 Multi Wavelength Section

Figure 11 shows the multi wavelength data of WISE J093141.09+023616.2. The flux density is plotted against the frequency of the detected photons. The object can be classified by comparing the data to the general SED in figure 2 from P. Padovani et al. (2017). Starting with the radio band, the data from the surveys FIRST (White et al., 1997), NVSS (Condon et al., 1998), CLASSSCAT (Myers et al., 2003), GB6 (Gregory et al., 2001) and PMN (Griffith et al., 1994) in figure 11 show a steep increase in flux. Comparing this to the radio band in figure 2, it shows that the observed object most likely possesses a jet. A non-jetted AGN would show a much softer rise in flux. Fitting the data between the radio and infrared band yields a peak at a frequency $\sim 10^{13}$ Hz which corresponds to a low synchrotron peaked AGN (Compare figure 3).
At frequencies between 10^{14} and 10^{15} Hz, the SED shows a narrow peak. Figure 2 shows, that this corresponds to the emission of the accretion disk that is shown as a thick blue line. This emission generally peaks in the far optical and UV band and is therefore called the big blue bump (P. Padovani et al., 2017). However, this emission could also be due to emission from the host galaxy. Unfortunately, without a secure estimate of the distance of the object, no reliable statement about the origin can be done. At frequencies below the big blue bump, the flux in figure 2 seems to rise. Comparison with the general SED makes it clear, that this rise is due to the emission from the dusty torus around the AGN that is shown in figure 1.
Radiation emitted by the accretion disk passes through the dusty torus and is partly absorbed. The rest of the radiation that interacts with the particles in the torus is reprocessed and re-emitted in a lower energy band. Since the emission from the accretion

disk is prominent, it is plausible that there also is strong emission from the dusty torus in the mid to far infrared. This is of course dependent on the position of the observer. If the object was observed from the where the torus is between the observer and the nucleus, the dusty torus would absorb most of the emission in this direction and the SED would show no flux at this band. In a blazar, the emission of the jet mostly dominates the SED. In this case however, the jet emission is only visible in the radio band, where no other mechanism contributes to the emission.
This leads to the conclusion that the object has a jet which is however not very dominant. Thus, the emission of other parts of the AGN such as the accretion disk are the prominent features that dominate the SED. Following the assumption that the object is a low synchrotron peaked AGN, shows that the flux at high γ-rays is very low. This is consistent with the *Fermi* analysis that yields no detectable flux in this energy band. Figure 2 also shows that the second peak of the jet emission would have its maximum in the low energy γ-ray band i.e. in the MeV band. As mentioned in section 2.1, there are no currently operating missions that observe the sky at these energies, therefore there is no way to observe the second peak in the near future. The x-ray data from eROSITA is at low keV energies, which corresponds to a frequency of $\sim 10^{18}$ Hz. Comparing this to figure 2 shows that this emission is most likely due to the jet or the hot corona around the accretion disk. The data is too sparse to be sure what the origin of this emission is.
The SED in general has a lot of gaps where no data points are acquired, mostly due to a poor coverage at energies like MeV. Section 5 gives an overview on what can be done in the future to improve our knowledge of this object.

5 Future Perspectives

The sections up until now show the analysis that was done so far to classify the object WISE J093141.09+023616.2. It is the same procedure that is done to analyse other potential neutrino counterparts. However, there still is much work to do to be able to create a complete picture of the properties of the object. The final goal is to shed light at the likelihood that the neutrino IceCube-200615A originates from this source.
The first thing that has to be clarified is the redshift. In section 3.2 the difference between photometric and spectroscopic redshift was explained. The photometric redshift listed in the eFEDS AGN catalog $z = 1.914$ is not reliable for further analysis that requires the redshift. An optical telescope could be used to observe the object and create the optical spectrum. The emission and absorption lines in the optical spectrum are also shifted by the redshift of the object. Since the rest-frame positions of the lines are known, the redshift can be determined much more reliably than photometrically.
The optical spectrum also provides more insight about the class of AGN the object belongs to. For example, if the object is a BL Lac, the optical spectrum would show no emission lines and the spectrum would be featureless. Additionally, the spectrum provides the flux at 4400Å which is needed to determine whether the source truly is radio-

loud or radio-quiet. For now, it is quite promising to be a radio-loud object since a non-jetted AGN would not have such a steep increase in flux in the radio band that can be seen in figure 11. Information about the type of object can also be obtained from the morphology of the host galaxy (e.g. elliptic galaxies in general contain more radio-loud AGN than spiral galaxies).
Besides the optical spectrum, the X-ray spectrum can also be determined. This helps to identify the origin of the emission in the X-ray band in figure 11. Figure 2 shows in the X-rays that we have a steeply rising component that comes from the LSP jet and a more or less constant part that comes from the hot corona around the accretion disk. Obtaining the slope of the X-ray spectrum would give more information about the origin of the X-ray emission. Another important quantity that can be computed is the bolometric luminosity L of the object. It describes the energy that is emitted through radiation per second. The bolometric luminosity is an intrinsic property of an astrophysical object and in contrary to the flux not dependent on the position of the observer. Therefore, the distance to the object has to be known. Since the redshift is a measure of how long a photon has been travelling, it can be used to determine the distance R to its origin. The luminosity can then be calculated by integrating the flux S_γ over the surface of a sphere with radius R to get the monochromatic luminosity $L(\nu)$ at a certain frequency. Integrating the monochromatic luminosity over all frequencies, the bolometric luminosity of an object is obtained (Gabriele Ghisellini, 2013)

$$L = \int_0^\infty L(\nu)\, d\nu \tag{7}$$

Especially the luminosity in the X-ray and optical band can be used to gather information about the mechanisms behind the energy generation in AGN, Lusso and Risaliti (2016) suggests.
In section 4.4 it is mentioned that the peak of the second hump of the jet emission probably lies somewhere in the MeV band where no data is available. Therefore, it has to be waited for potential future missions that cover the MeV band like AMEGO-X. AMEGO-X will cover the energy band between high X-rays and high γ-rays and close the gap between X-ray missions like eROSITA and the *Fermi* LAT. This is especially interesting in the aspect of multi-messenger astronomy because sources of neutrinos and gravitational waves also produce photons in the γ-rays (Fleischhack, 2021).
Another interesting future mission is the Imaging X-ray Polarimetry Explorer (IXPE). IXPE will launch in late 2021 and will observe the X-ray sky at energies between 2 and 8 keV. It also detects the polarization of the X-ray emission which improves the understanding of X-ray producing astrophysical objects like AGN (Soffitta, 2017).
The eFEDS field in general with its more than twenty-thousand possible AGN is an interesting region in the sky for further analysis of AGN. Figure 13 shows the eFEDS field and the AGN observed by eROSITA as cyan dots. The points in other colours mark AGN that are included in catalogs that only include radio-loud AGN or radio-loud candidate AGN. These objects are especially interesting for future work since they

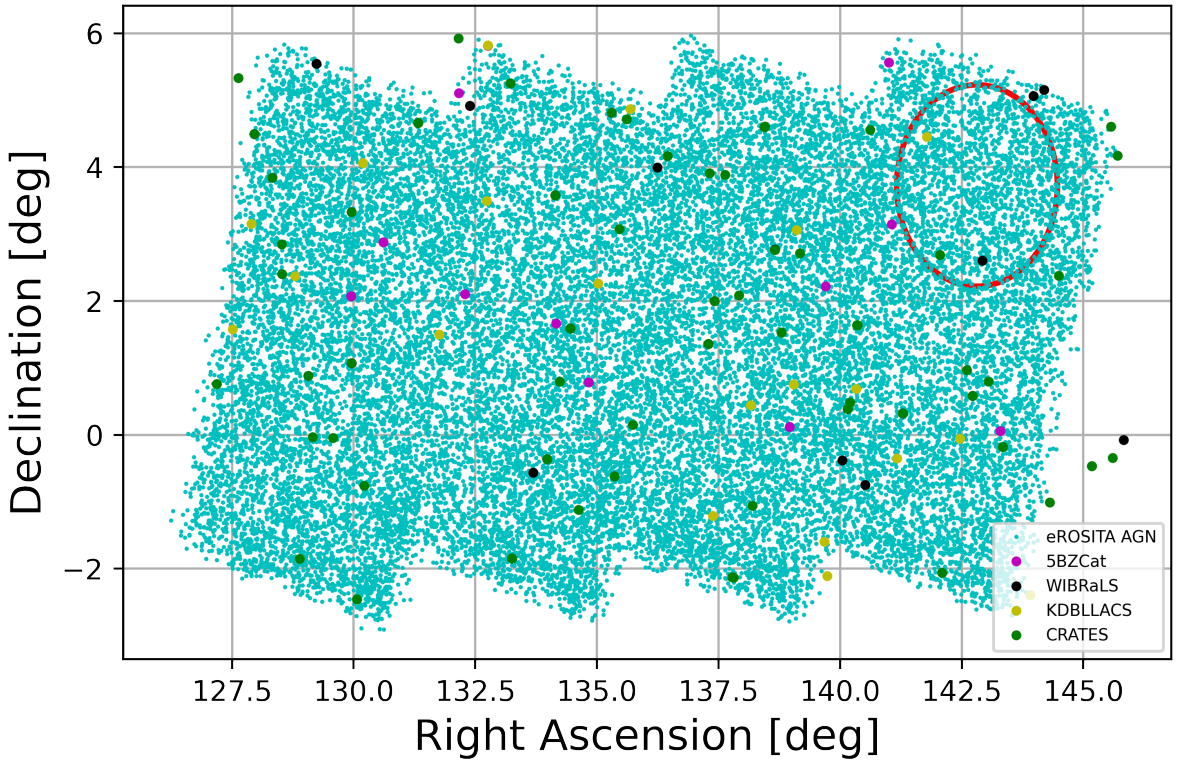

Figure 13: eFEDS field with all AGN observed by eROSITA marked in cyan. The dots in other colours mark AGN that are listed in catalogs that only include radio-loud AGN or radio-loud candidate AGN. Radio-loud AGN are especially interesting for this work since they are jetted AGN and this work focuses on neutrino producing processes in the jet.

are already classified. The red ellipse marks the neutrino positional error region with the candidate radio-loud sources that are discussed in section 4.2 in it.

6 Conclusion

Out of all the AGN that are within the positional error of the neutrino IceCube-200615A, the WISE source J093141.09+023616.2 was chosen for further analysis. This is due to the fact that it is the only source that is classified as a radio-loud AGN by the catalogs WIBRaLS, KDBLLACS and 5BZCat. It lies within the positional uncertainty of one of the eROSITA AGN in eFEDS that provides data in the X-rays. There are numerous missions that provide data in other bands of the electromagnetic spectrum that were used to plot the spectral energy distribution of the object (Figure 11). The SED shows that the object most likely is a radio-loud source as WIBRaLS already suggested. This can be seen in the radio band where the data points show a steep rise. However, the jet probably is not very dominant at higher frequencies. Especially in the infrared and optical, the big blue bump can be seen that shows the emission of the accretion disk (e.g. figure 2). Right before the big blue bump, at a frequency around 10^{13} Hz, the data rises again which is due to the reprocessing of the accretion disk emission in the dusty torus. The emission in the X-ray band from eROSITA has no clear origin. it could be due to the jet or emission from the hot corona around the accretion disk. None of the *Fermi*-LAT catalogs up to the newest 10-year survey included an object in accordance with WISE J093141.09+023616.2. Therefore, an upper limit for the flux was calculated that gives a limit how bright the object has to be in the γ-rays to be detected by the *Fermi*-LAT. The upper limit was calculated to be $S_\gamma = 1.4 \times 10^{-12} \, \frac{\text{erg}}{\text{cm}^2\text{s}}$.
There is still a lot of work that can be done to learn more about this source and whether it could be the origin of the neutrino. Section 5 deals in detail with the next steps of the analysis that have to be performed. In conclusion, the source WISE J093141.09+023616.2 is a very interesting object and candidate counterpart for the neutrino detection IceCube-200615A that is worth to be further looked into.

7 Acknowledgement

I want to thank Sara Buson for the opportunity to perform the analysis and work with her. She also helped me improve my understanding of AGN and astronomy in general. It is easy to get lost in all the different catalogs of astrophysical sources. I am glad and thankful that Raniere de Menezes provided me the most important ones and helped me navigate through them with his expertise.
In addition to that, I would like to thank the other members of our group for all the constructive feedback they gave.
I also thank all the people who proof-read my thesis and made sure there are no stupid mistakes.
Finally, my special thanks go to my family and my girlfriend who supported me all the way through and always believed in me.

References

Aartsen, M.G., M. Ackermann, J. Adams, J.A. Aguilar, M. Ahlers, M. Ahrens, D. Altmann, K. Andeen, T. Anderson, I. Ansseau, and et al. (Mar. 2017). "The IceCube Neutrino Observatory: instrumentation and online systems". In: *Journal of Instrumentation* 12.03, P03012–P03012. ISSN: 1748-0221. DOI: 10.1088/1748-0221/12/03/p03012. URL: http://dx.doi.org/10.1088/1748-0221/12/03/P03012.

Abdo, A. A. et al. (May 2010). "THE SPECTRAL ENERGY DISTRIBUTION OFFERMIB-RIGHT BLAZARS". In: *The Astrophysical Journal* 716.1, pp. 30–70. DOI: 10.1088/0004-637x/716/1/30. URL: https://doi.org/10.1088/0004-637x/716/1/30.

Abdollahi, S., F. Acero, M. Ackermann, M. Ajello, W. B. Atwood, M. Axelsson, L. Baldini, J. Ballet, G. Barbiellini, D. Bastieri, and et al. (Mar. 2020). "Fermi Large Area Telescope Fourth Source Catalog". In: *The Astrophysical Journal Supplement Series* 247.1, p. 33. ISSN: 1538-4365. DOI: 10.3847/1538-4365/ab6bcb. URL: http://dx.doi.org/10.3847/1538-4365/ab6bcb.

Atwood, W. B., A. A. Abdo, M. Ackermann, W. Althouse, B. Anderson, M. Axelsson, L. Baldini, J. Ballet, D. L. Band, G. Barbiellini, and et al. (May 2009). "THE LARGE AREA TELESCOPE ON THEFERMI GAMMA-RAY SPACE TELESCOPEMISSION". In: *The Astrophysical Journal* 697.2, pp. 1071–1102. ISSN: 1538-4357. DOI: 10.1088/0004-637x/697/2/1071. URL: http://dx.doi.org/10.1088/0004-637X/697/2/1071.

Beckmann, Volker and Chris R. Shrader (2013). *The AGN phenomenon: open issues*. arXiv: 1302.1397 [astro-ph.HE].

Blanton, Michael R. et al. (July 2017). "Sloan Digital Sky Survey IV: Mapping the Milky Way, Nearby Galaxies, and the Distant Universe". In: 154.1, 28, p. 28. DOI: 10.3847/1538-3881/aa7567. arXiv: 1703.00052 [astro-ph.GA].

Brunner, H. et al. (2021). *The eROSITA Final Equatorial Depth Survey (eFEDS): The X-ray catalog*. arXiv: 2106.14517 [astro-ph.HE].

Condon, J. J., W. D. Cotton, E. W. Greisen, Q. F. Yin, R. A. Perley, G. B. Taylor, and J. J. Broderick (May 1998). "The NRAO VLA Sky Survey". In: 115.5, pp. 1693–1716. DOI: 10.1086/300337.

D'Abrusco, Raffaele, Nuria Álvarez Crespo, Francesco Massaro, Riccardo Campana, Vahram Chavushyan, Marco Landoni, Fabio La Franca, Nicola Masetti, Dan Milisavljevic, Alessandro Paggi, and et al. (May 2019). "Two New Catalogs of Blazar Candidates in the WISE Infrared Sky". In: *The Astrophysical Journal Supplement Series* 242.1, p. 4. ISSN: 1538-4365. DOI: 10.3847/1538-4365/ab16f4. URL: http://dx.doi.org/10.3847/1538-4365/ab16f4.

Dey, Arjun et al. (May 2019). "Overview of the DESI Legacy Imaging Surveys". In: *The Astrophysical Journal* 157.5, 168, p. 168. DOI: 10.3847/1538-3881/ab089d. arXiv: 1804.08657 [astro-ph.IM].

Fleischhack, Henrike (2021). *AMEGO-X: MeV gamma-ray Astronomy in the Multimessenger Era*. arXiv: 2108.02860 [astro-ph.IM].

Ghisellini, G., L. Maraschi, and F. Tavecchio (June 2009). "The Fermi blazars' divide". In: *Monthly Notices of the Royal Astronomical Society: Letters* 396.1, pp. L105–L109. ISSN: 1745-3925. DOI: 10.1111/j.1745-3933.2009.00673.x. eprint: https://academic.oup.com/mnrasl/article-pdf/396/1/L105/3024240/396-1-L105.pdf. URL: https://doi.org/10.1111/j.1745-3933.2009.00673.x.

Ghisellini, Gabriele (2013). "Radiative Processes in High Energy Astrophysics". In: *Lecture Notes in Physics*. ISSN: 1616-6361. DOI: 10.1007/978-3-319-00612-3. URL: http://dx.doi.org/10.1007/978-3-319-00612-3.

Gregory, P. C., P. Capak, D. Gasson, and W. K. Scott (Jan. 2001). "The GB6 4.85 GHz radio variability catalog". In: *Galaxies and their Constituents at the Highest Angular Resolutions*. Ed. by R. T. Schilizzi. Vol. 205, p. 98.

Griffith, Mark R., Alan E. Wright, B. F. Burke, and R. D. Ekers (Jan. 1994). "The Parkes-MIT-NRAO (PMN) Surveys. III. Source Catalog for the Tropical Survey (-29 degrees < delta < -9 degrees -3pt.5)". In: 90, p. 179. DOI: 10.1086/191863.

Healey, Stephen E., Roger W. Romani, Gregory B. Taylor, Elaine M. Sadler, Roberto Ricci, Tara Murphy, James S. Ulvestad, and Joshua N. Winn (July 2007). "CRATES: An All-Sky Survey of Flat-Spectrum Radio Sources". In: 171.1, pp. 61–71. DOI: 10.1086/513742. arXiv: astro-ph/0702346 [astro-ph].

Hovatta, T., Lindfors, E., Kiehlmann, S., Max-Moerbeck, W., Hodges, M., Liodakis, I., Lähteemäki, A., Pearson, T. J., Readhead, A. C. S., Reeves, R. A., Suutarinen, S., Tammi, J., and Tornikoski, M. (2021). "Association of IceCube neutrinos with radio sources observed at Owens Valley and Metsähovi Radio Observatories". In: *A&A* 650, A83. DOI: 10.1051/0004-6361/202039481. URL: https://doi.org/10.1051/0004-6361/202039481.

IceCube Collaboration et al. (July 2018). "Neutrino emission from the direction of the blazar TXS 0506+056 prior to the IceCube-170922A alert". In: *Science* 361.6398, pp. 147–151. DOI: 10.1126/science.aat2890. arXiv: 1807.08794 [astro-ph.HE].

Katz, U.F. and Ch. Spiering (July 2012). "High-energy neutrino astrophysics: Status and perspectives". In: *Progress in Particle and Nuclear Physics* 67.3, pp. 651–704. ISSN: 0146-6410. DOI: 10.1016/j.ppnp.2011.12.001. URL: http://dx.doi.org/10.1016/j.ppnp.2011.12.001.

Liu, A. et al. (2021). *The eROSITA Final Equatorial-Depth Survey (eFEDS): Catalog of galaxy clusters and groups*. arXiv: 2106.14518 [astro-ph.CO].

Liu, Teng et al. (2021). *The eROSITA Final Equatorial-Depth Survey (eFEDS): The AGN Catalogue and its X-ray Spectral Properties*. arXiv: 2106.14522 [astro-ph.HE].

Lusso, E. and G. Risaliti (Mar. 2016). "THE TIGHT RELATION BETWEEN X-RAY AND ULTRAVIOLET LUMINOSITY OF QUASARS". In: *The Astrophysical Journal* 819.2, p. 154. ISSN: 1538-4357. DOI: 10.3847/0004-637x/819/2/154. URL: http://dx.doi.org/10.3847/0004-637X/819/2/154.

Massaro, E., P. Giommi, C. Leto, P. Marchegiani, A. Maselli, M. Perri, S. Piranomonte, and S. Sclavi (Dec. 2008). "Roma-BZCAT: a multifrequency catalogue of blazars". In: *Astronomy & Astrophysics* 495.2, pp. 691–696. ISSN: 1432-0746. DOI: 10.1051/

0004-6361:200810161. URL: http://dx.doi.org/10.1051/0004-6361:200810161.

Mastichiadis, Apostolos and Maria Petropoulou (Jan. 2021). "Hadronic X-Ray Flares from Blazars". In: *The Astrophysical Journal* 906.2, p. 131. ISSN: 1538-4357. DOI: 10.3847/1538-4357/abc952. URL: http://dx.doi.org/10.3847/1538-4357/abc952.

Menezes, Raniere de, Harold A. Peña-Herazo, Ezequiel J. Marchesini, Raffaele D'Abrusco, Nicola Masetti, Rodrigo Nemmen, Francesco Massaro, Federica Ricci, Marco Landoni, Alessandro Paggi, and et al. (Sept. 2019). "Optical characterization of WISE selected blazar candidates". In: *Astronomy & Astrophysics* 630, A55. ISSN: 1432-0746. DOI: 10.1051/0004-6361/201936195. URL: http://dx.doi.org/10.1051/0004-6361/201936195.

Murase, Kohta, Dafne Guetta, and Markus Ahlers (Feb. 2016). "Hidden Cosmic-Ray Accelerators as an Origin of TeV-PeV Cosmic Neutrinos". In: *Physical Review Letters* 116.7. ISSN: 1079-7114. DOI: 10.1103/physrevlett.116.071101. URL: http://dx.doi.org/10.1103/PhysRevLett.116.071101.

Myers, S. T., N. J. Jackson, I. W. A. Browne, A. G. de Bruyn, T. J. Pearson, A. C. S. Readhead, P. N. Wilkinson, A. D. Biggs, R. D. Blandford, C. D. Fassnacht, L. V. E. Koopmans, D. R. Marlow, J. P. McKean, M. A. Norbury, P. M. Phillips, D. Rusin, M. C. Shepherd, and C. M. Sykes (May 2003). "The Cosmic Lens All-Sky Survey - I. Source selection and observations". In: 341.1, pp. 1–12. DOI: 10.1046/j.1365-8711.2003.06256.x. arXiv: astro-ph/0211073 [astro-ph].

Padovani, P., D. M. Alexander, R. J. Assef, B. De Marco, P. Giommi, R. C. Hickox, G. T. Richards, V. Smolčić, E. Hatziminaoglou, V. Mainieri, and et al. (Aug. 2017). "Active galactic nuclei: what's in a name?" In: *The Astronomy and Astrophysics Review* 25.1. ISSN: 1432-0754. DOI: 10.1007/s00159-017-0102-9. URL: http://dx.doi.org/10.1007/s00159-017-0102-9.

Plavin, A. V., Y. Y. Kovalev, Yu. A. Kovalev, and S. V. Troitsky (Feb. 2021). "Directional Association of TeV to PeV Astrophysical Neutrinos with Radio Blazars". In: *The Astrophysical Journal* 908.2, p. 157. ISSN: 1538-4357. DOI: 10.3847/1538-4357/abceb8. URL: http://dx.doi.org/10.3847/1538-4357/abceb8.

Predehl, P. (June 2014). "eROSITA – Mapping the X-ray universe". In: *Astronomische Nachrichten* 335. DOI: 10.1002/asna.201412059.

Salvato, M. et al. (2021). *The eROSITA Final Equatorial-Depth Survey (eFEDS): Identification and characterization of the counterparts to the point-like sources*. arXiv: 2106.14520 [astro-ph.HE].

Soffitta, Paolo (Aug. 2017). "IXPE the Imaging X-ray Polarimetry Explorer". In: *Society of Photo-Optical Instrumentation Engineers (SPIE) Conference Series*. Vol. 10397. Society of Photo-Optical Instrumentation Engineers (SPIE) Conference Series, p. 103970I. DOI: 10.1117/12.2275485.

Urry, C. Megan and Paolo Padovani (Sept. 1995). "Unified Schemes for Radio-Loud Active Galactic Nuclei". In: *Publications of the Astronomical Society of the Pacific* 107, p. 803. DOI: 10.1086/133630. URL: https://doi.org/10.1086/133630.

White, Richard L., Robert H. Becker, David J. Helfand, and Michael D. Gregg (Feb. 1997). "A Catalog of 1.4 GHz Radio Sources from the FIRST Survey". In: 475.2, pp. 479–493. DOI: 10.1086/303564.

Yuan, Chengchao, Kohta Murase, and Peter Mészáros (Feb. 2020). "Complementarity of Stacking and Multiplet Constraints on the Blazar Contribution to the Cumulative High-energy Neutrino Intensity". In: 890.1, 25, p. 25. DOI: 10.3847/1538-4357/ab65ea. arXiv: 1904.06371 [astro-ph.HE].

Zhao, Gang, Yongheng Zhao, Yaoquan Chu, Yipeng Jing, and Licai Deng (2012). *LAMOST Spectral Survey*. arXiv: 1206.3569 [astro-ph.IM].

Eidesstattliche Erklärung

Hiermit versichere ich, die vorliegende Arbeit selbstständig verfasst und keine anderen als die angegebenen Quellen und Hilfsmittel benutzt sowie die Zitate deutlich kenntlich gemacht zu haben.
Ich erkläre weiterhin, dass die vorliegende Arbeit in gleicher oder ähnlicher Form noch nicht im Rahmen eines anderen Prüfungsverfahrens eingereicht wurde.

Würzburg, den 10. Januar 2023 Lenz Oswald